



# Spiking at the edge: Excitability at interfaces in reaction–diffusion systems

Colin Scheibner<sup>ab</sup>, Hillel Ori<sup>c</sup>, Adam E. Cohen<sup>cd</sup>, and Vincenzo Vitelli<sup>a,b,e,1</sup>

Edited by Jacques Prost, Institut Curie, Paris, France; received May 12, 2023; accepted October 25, 2023 by Editorial Board Member Paul Chaikin

Excitable media, ranging from bioelectric tissues and chemical oscillators to forest fires and competing populations, are nonlinear, spatially extended systems capable of spiking. Most investigations of excitable media consider situations where the amplifying and suppressing forces necessary for spiking coexist at every point in space. In this case, spikes arise due to local bistabilities, which require a fine-tuned ratio between local amplification and suppression strengths. But, in nature and engineered systems, these forces can be segregated in space, forming structures like interfaces and boundaries. Here, we show how boundaries can generate and protect spiking when the reacting components can spread out: Even arbitrarily weak diffusion can cause spiking at the edge between two non-excitable media. This edge spiking arises due to a global bistability, which can occur even if amplification and suppression strengths do not allow spiking when mixed. We analytically derive a spiking phase diagram that depends on two parameters: i) the ratio between the system size and the characteristic diffusive length-scale and ii) the ratio between the amplification and suppression strengths. Our analysis explains recent experimental observations of action potentials at the interface between two non-excitable bioelectric tissues. Beyond electrophysiology, we highlight how edge spiking emerges in predator–prey dynamics and in oscillating chemical reactions. Our findings provide a theoretical blueprint for a class of interfacial excitations in reaction–diffusion systems, with potential implications for spatially controlled chemical reactions, nonlinear waveguides and neuromorphic computation, as well as spiking instabilities, such as cardiac arrhythmias, that naturally occur in heterogeneous biological media.

reaction–diffusion equations | dynamical systems | electrophysiology | morphogenesis | topological phenomena

A spike is a large nonlinear excursion in a dynamical system followed by a time of latency known as the refractory period. Protecting the ability to spike is crucial for a wide range of biological functions, from cardiac pacemaking (1–6) to neural information processing (7), while in other contexts, such as forest fires (8) and disease outbreaks (9–12), spiking is undesirable. In a spatially extended medium, the ability to spike gives rise to distinctive spatiotemporal patterns (13–23) appearing in processes ranging from morphogenesis (24–34) to spiral waves observed in electrograms of the heart (35–37). While analytical studies have revealed important features of excitable media whose properties are spatially homogeneous (38–42), less is understood about abrupt heterogeneities such as sample edges or interfaces (43–54). As is often the case with wave mechanics, edges and interfaces can have properties that differ qualitatively from those of the bulk medium (55–61).

For instance, Fig. 1*A* shows a recent experiment in which human embryonic kidney (HEK293) cells were genetically modified to express either sodium ( $\text{Na}_v1.5$ ) or potassium ( $\text{K}_{ir2.1}$ ) channels (63). Usually, a cell containing both potassium and sodium channels spikes via the following mechanism, which is representative of excitable systems: The potassium channels favor a low membrane potential, while the sodium channels favor a high membrane potential, creating a bistability. Given a suitably large voltage stimulation, the membrane potential (a fast variable) spikes upward toward the value set by the sodium channels. The sodium channels then gradually shut due to open-state inactivation (a slow variable), causing the membrane potential to fall toward the value set by the potassium channels. The sodium channels then take some time to recover their strength (the refractory period). Because the competition between the two channels is essential, neither sodium nor potassium channels alone are sufficient for an individual cell to spike. Furthermore, even when both channels coexist in a single cell, spikes only occur when they have the appropriate ratio of open-state conductances (i.e., channel strengths).

## Significance

Spiking is a general phenomenon that is crucial in the firing of neurons, beating of hearts, and spread of diseases. In homogeneous media, spiking arises from a local competition between amplifying and suppressing forces. But most real-world systems are far from homogeneous. Here, we demonstrate that inhomogeneities such as interfaces and boundaries (that spatially segregate these two forces) can promote spiking, even if the system does not spike when these forces are evenly mixed. We mathematically derive a spiking phase diagram in terms of interfacial diffusion and amplification strength. Our findings apply to chemical reactions, predator–prey dynamics, and recent electrophysiology experiments, in which localized action potentials were observed at the interface of distinct, nonspiking bioelectric tissues.

Author contributions: C.S., H.O., A.E.C., and V.V. designed research; C.S., H.O., A.E.C., and V.V. performed research; C.S. and H.O. analyzed data; and C.S., H.O., A.E.C., and V.V. wrote the paper.

The authors declare no competing interest.

This article is a PNAS Direct Submission. J.P. is a guest editor invited by the Editorial Board.

Copyright © 2024 the Author(s). Published by PNAS. This article is distributed under [Creative Commons Attribution-NonCommercial-NoDerivatives License 4.0 \(CC BY-NC-ND\)](https://creativecommons.org/licenses/by-nc-nd/4.0/).

<sup>1</sup>To whom correspondence may be addressed. Email: vitelli@uchicago.edu.

This article contains supporting information online at <https://www.pnas.org/lookup/suppl/doi:10.1073/pnas.2307996120/-/DCSupplemental>.

Published January 12, 2024.

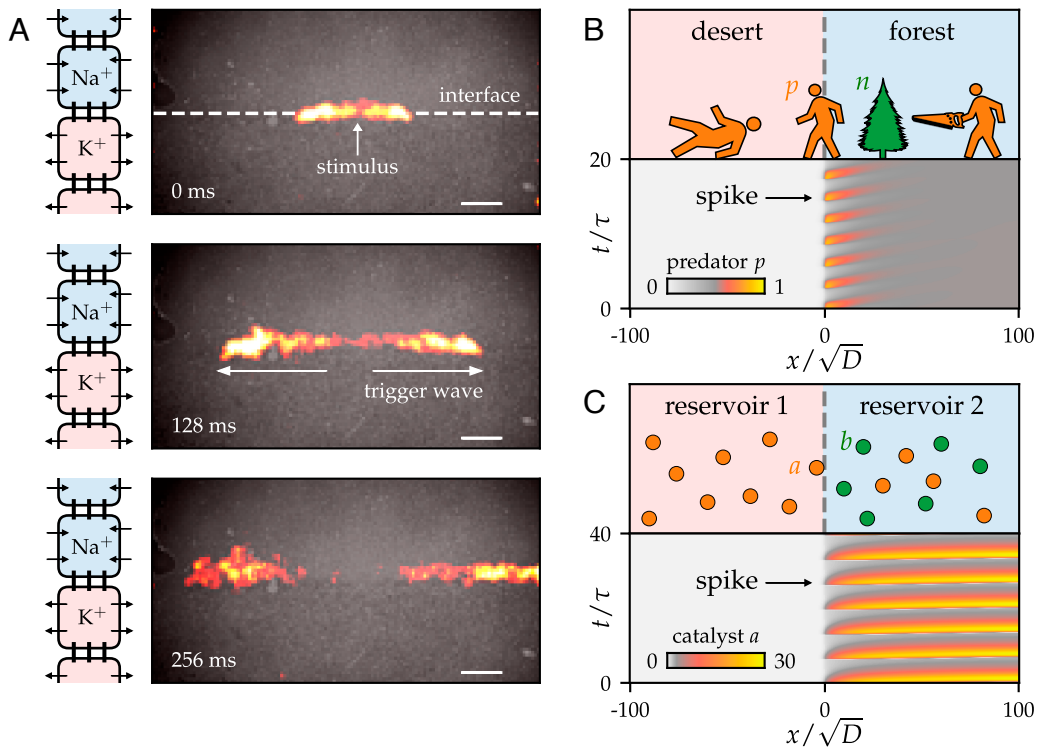


**Fig. 1.** Edge spiking in electrophysiology, population dynamics, and chemistry. (A) Experiments from ref. 63 in which an action potential propagates along a tissue interface, as revealed by a voltage-sensitive red dye. See [Movie S1](#). (Scale bar, 1 mm). The *Left* column shows a schematic vertical cross-section of the interface: The top tissue features sodium ion channels (inward arrows), while the bottom tissue features potassium ion channels (outward arrows). The vertical lines represent gap junction coupling between the cells. Images adapted from ref. 63. (B) A fast diffusing predator (lumberjacks) and relatively immobile prey (trees) are described by an interfacial Lotka–Volterra model [Eqs. 3 and 4]. A kymograph generated by the model reveals spikes in the lumberjack population at the interface. (C) An interface between two chemical reservoirs, neither of which are capable of oscillating, is described by Eqs. 10 and 11. A kymograph of the fast, mobile catalyst  $a$  reveals repeated spikes generated at the interface.

Something visually striking happens when two distinct and non-excitable tissues (composed of the two cell types) are placed in contact and weakly coupled by gap junctions, which allow voltage diffusion. When stimulated at the interface, a voltage spike (i.e., an action potential) emerges and robustly propagates along the interface; see Fig. 1A and [Movie S1](#) (62). Crucially, these interfacial spikes persist for a much wider range of open-state conductances than for a single cell (63). This observation suggests that spikes generated at an interface may have a distinct, and possibly more robust, dynamical origin than those in a homogenized system. Here, we reveal the underlying dynamical mechanism behind this phenomenon and demonstrate that it is not limited to electrophysiology. For instance, we provide examples from population dynamics (Fig. 1B) in which a fast, mobile predator (lumberjacks) consumes a slow, sedentary prey (trees) while diffusing across an environmental (forest–desert) boundary, and from chemical reaction networks in which a fast catalyst diffuses between two chemically distinct reservoirs (Fig. 1C). In all these examples, a spiking interface is more than the sum of its parts: Interfacial spiking does not result from merely superimposing the two halves. In fact, coupling the two halves too strongly can destroy spiking altogether.

## Results

**Spiking Boundaries and the Role of Spatial Extent.** The basic notion of an edge spike involves two distinct processes: transport across two domains and transport within the domains themselves. To illustrate the former, consider a two-compartment model of predator–prey dynamics shown in Fig. 2A, *Inset*. The model features a population  $p$  of lumberjacks (the predators) that

consumes a population  $n$  of trees (the prey). The rightmost compartment, the forest (blue bar), acts as a lumberjack amplifier in which tree consumption elevates the lumberjack population. By contrast, the desert (red bar) is an infinitely strong suppressor in which any lumberjack that enters dies instantly. Lumberjacks from the forest wander into the adjacent desert with a hopping rate  $\epsilon$ . The populations evolve according to the following Lotka–Volterra equation:

$$\dot{p} = -\epsilon p + npk(p), \quad [1]$$

$$\dot{n} = \frac{n}{\tau} \left( 1 - n - \frac{p}{q} \right), \quad [2]$$

where  $1/q$  is the predation rate,  $\tau \gg 1$  is a long time scale implying that the tree population changes slowly, and  $k(p)$  is a nonlinearity that encodes a lumberjack carrying capacity. A normalization has been chosen so that all variables in Eqs. 1 and 2 are dimensionless and the carrying capacities of the lumberjacks and trees are set to 1; see [SI Appendix section 1](#). Here, the lumberjack population plays the same role as the cell-membrane potential in the electrophysiology experiment (a fast, diffusing variable), the tree population corresponds to the gating variable of the sodium channels (an immobile, slow variable), while the desert and the forest correspond to cells with potassium and sodium channels, respectively.

In this model, the ability to spike depends sensitively on the hopping rate  $\epsilon$ . If  $\epsilon = 0$  (Fig. 2A), the two halves are decoupled and the lumberjack population cannot spike: The lumberjacks will quickly return to their carrying capacity regardless of the perturbation. However, when  $\epsilon$  is small but nonzero (Fig. 2B), the dynamics change dramatically: The lumberjacks can now

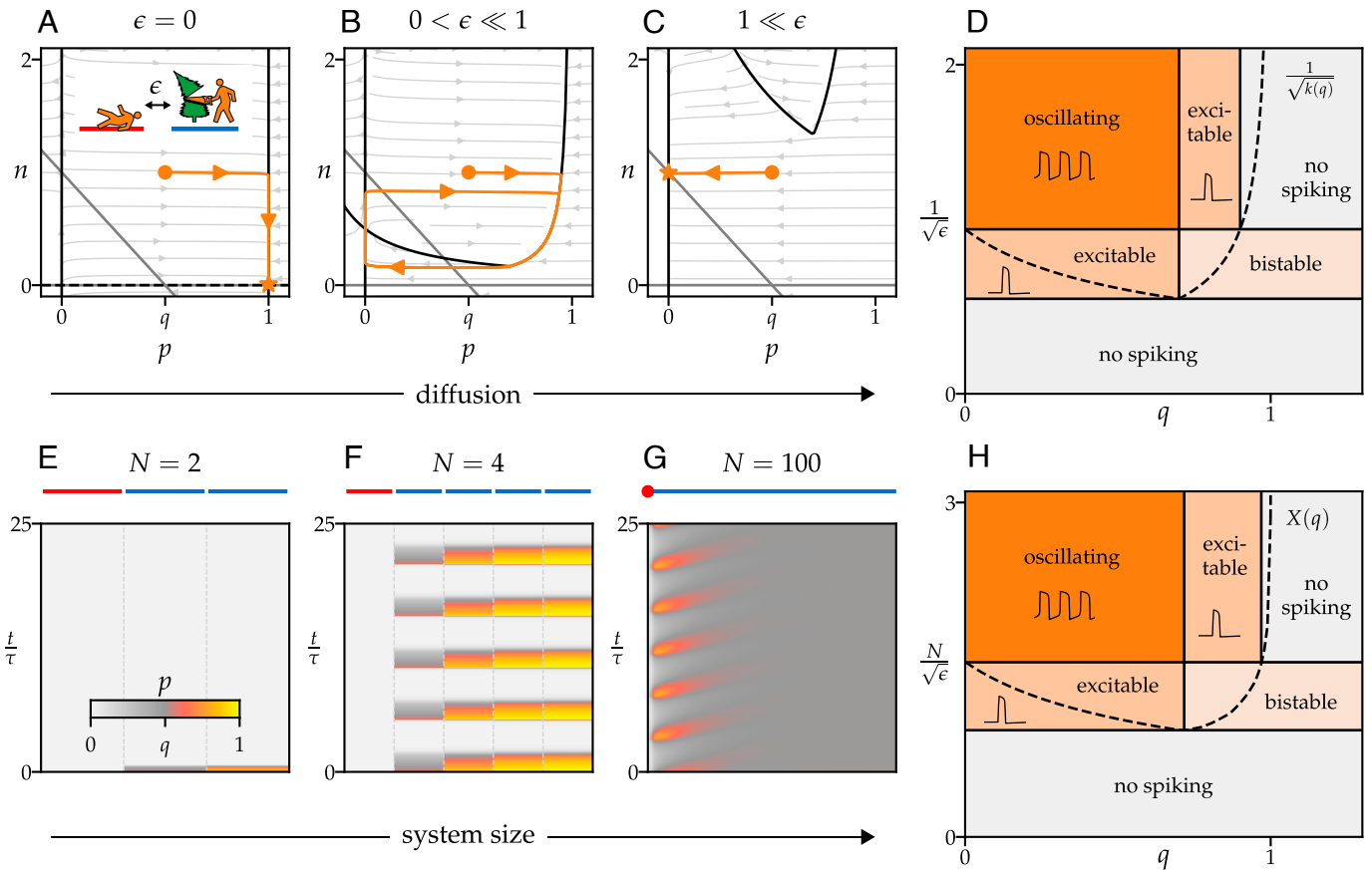


**Fig. 2.** Spikes induced by weak diffusion and large system size. (A) (*Inset*) A predator–prey system with a desert (red) and a forest (blue) described by Eqs. 1 and 2. In the forest, the predators (lumberjacks,  $p$ ) consume the prey (trees,  $n$ ) with predation rate  $1/q$ . The predators cross from the forest to the desert (and subsequently perish) with hopping rate  $\epsilon$ . (A–C) Three phase portraits, for  $\epsilon = 0$ ,  $0 < \epsilon \ll 1$ , and  $1 \ll \epsilon$ , illustrate the role of diffusion across a boundary: For  $\epsilon = 0$  (A), the lumberjacks reach their carrying capacity and the trees go extinct. For  $\epsilon \ll 1$  (B), in which the effective death rate due to hopping is present but not overpowering, orange curves are example trajectories. The  $\dot{p} = 0$  and  $\dot{n} = 0$  nullclines are denoted by black and gray lines, respectively. (D) A phase diagram for Eqs. 1 and 2 summarizes the possible behaviors: If the lumberjack hopping rate  $\epsilon$  is too large, the lumberjack population cannot spike. The phase boundaries are determined by the consumption nonlinearity  $k(q)$  in Eqs. 1 and 2. (E–G) A chain of  $N$  forests (blue lines) are coupled to a desert (red line) by a large hopping rate  $\epsilon = 4$ . Kymographs for systems with  $N = 2$ ,  $N = 4$ , and  $N = 100$  exemplify a distinctive transition: Oscillation onset is driven by increasing system size, even as  $\epsilon$  is held constant. (See *SI Appendix section 1* for simulation details.) (H) A phase diagram for Eqs. 3 and 4, applicable for  $N \gg 1$ , reveals a crucial distinction between the spatially and non-spatially extended systems: The vertical axis in (H) features  $N/\sqrt{\epsilon}$ , implying that spiking occurs for a much larger range of  $\epsilon$  in the spatially extended limit. The curve  $X(q)$  determines the locations of the phase boundaries and is given in Eq. 21.

spike because the motion into the desert depletes the lumberjack population when trees are sparse and tree consumption overpowers diffusion when trees are abundant. Crucially, though, when  $\epsilon$  becomes too large (Fig. 2C), the desert and forest become well mixed, and the lumberjack population cannot spike because the suppressor (desert) is infinitely strong. In the two-compartment model described by Eqs. 3 and 4, the hopping rate  $\epsilon$  can be reinterpreted as an effective suppression strength: Even though the desert itself is infinitely strong, the finite entrance rate attenuates its effect. The phase diagram in Fig. 2D illustrates a basic mechanism: An amplifier and a suppressor need to be suitably well balanced for spikes to occur—attenuating a strong suppressor through weak diffusion across an interface helps achieve this balance.

Yet, this simplified model lacks a basic feature: the forest itself can be spatially extended. In Fig. 2E–G, the desert is now connected to a chain of  $N$  compartments comprising the forest, each of which is coupled to its neighbors by a hopping rate  $\epsilon$ . The size of the forest dramatically influences the dynamics. When  $N = 2$  and  $\epsilon = 4$ , the lumberjacks rapidly go extinct in all compartments (E). Yet, when  $N = 4$ , the lumberjack population

not only begins to survive but undergoes large oscillations (F). A window into the relationship between  $N$  and  $\epsilon$  can be obtained in the large  $N$  limit (G and H). In this limit, the dynamics can be described by a continuum reaction–diffusion equation:

$$\dot{p} = D\nabla^2 p + npk(p), \tag{3}$$

$$\dot{n} = \frac{n}{\tau} \left( 1 - n - \frac{p}{q} \right), \tag{4}$$

where  $L = Nd$  is the system size and  $d$  is the lattice spacing\*. The parameter  $D = \epsilon d^2$  denotes the diffusion coefficient times the characteristic time scale used to nondimensionalize  $\epsilon$  (*SI Appendix, section 1*). The lumberjack population obeys the following boundary conditions:  $\partial_x p = 0$  at  $x = L$  and, because of the infinitely strong desert,  $p = 0$  at  $x = 0$ . The basic effect of spatial extent can be obtained by dimensional analysis: Only  $\sqrt{D}$  and  $L$  have units of length, so any change in qualitative behavior

\* Notice that Eqs. 3 and 4 do not contain advective transport, which has also been shown to give rise oscillations near Dirichlet boundaries, for example, in models of and experiments on *Dictyostelium discoideum* (44, 45).

must depend on the dimensionless ratio  $L/\sqrt{D} = N/\sqrt{\epsilon}$ . Therefore, in the continuum, increasing  $N$  is equivalent to decreasing  $\epsilon$ . This collapse is physically consequential because the diffusion  $D$  is an intrinsic property of the material while  $L$  is an extrinsic property, so the two can often be tuned independently. Notably, by increasing  $L$  a system can support spiking over a wider range of  $D^\dagger$ .

**Interfaces and a Spiking Phase Diagram.** The dynamics are even richer when the suppressor (e.g., the desert) is no longer infinitely strong. In this case, the Dirichlet boundary becomes an interface, and spikes can arise both in the limit  $L/\sqrt{D} \rightarrow 0$  and  $L/\sqrt{D} \rightarrow \infty$ . To illustrate this behavior, we consider a one-dimensional (1D) model for the electrophysiology experiment of ref. 63 which takes the form of an interfacial Fitzhugh–Nagumo equation (64):

$$\dot{V} = D\nabla^2 V + \begin{cases} f_K(V) & x \in [-L, 0] \\ hf_{Na}(V) & x \in (0, L], \end{cases} \quad [5]$$

$$\dot{h} = \frac{h_\infty(V) - h}{\tau}. \quad [6]$$

Here,  $x$  is the coordinate transverse to the interface (Fig. 1A),  $V$  is the voltage, and  $f_K(V)$  and  $f_{Na}(V)$  capture the effect of the potassium and sodium channels, respectively. The sodium channels are modulated by a gating variable  $h$  that slowly approaches the function  $h_\infty(V)$  on a long time scale  $\tau$ . The term  $D\nabla^2 V$  arises from direct cell-to-cell current flow via gap junctions. Like the predator–prey system, a normalization is chosen such that the quantities  $\sqrt{D}$  and  $x$  have units of length, while all others are dimensionless (SI Appendix section 2). The system is modeled by no-flux boundary conditions at both ends,  $\partial_x V|_{\pm L} = 0$ , while the voltage  $V$  and its first derivative  $\partial_x V$  are required to be continuous across the interface.

The gating switch  $h_\infty(V)$  is reasonably well approximated by a step function  $h_\infty(V) = r\Theta(V_* - V)$ , where  $\Theta$  is a Heaviside step function and  $V_*$  is a crossover voltage that turns off the sodium channels (3). The parameter  $r$  is the ratio of the open-state conductances of the sodium to the potassium ion channels. Therefore,  $r$  can be interpreted as the relative strength of the amplifier (sodium) and suppressor (potassium). When  $r \ll 1$ , the potassium ion channels are so strong that the interface effective becomes a Dirichlet boundary of the type considered in the predator–prey system. When  $r \gg 1$ , both sides of the interface are dynamic.

In Fig. 3A and B, we sketch a three-dimensional phase diagram spanned by the parameters  $L/\sqrt{D}$ ,  $V_*$ , and  $r$ . When  $L/\sqrt{D} \rightarrow 0$ , diffusion forces the voltage to be approximately constant across the entire system, so we can think of the system as an effective single cell with both ion channels. By contrast, when  $L/\sqrt{D} \rightarrow \infty$ , the coupling is weak and the spatial heterogeneity plays a crucial role. To illustrate the independence of these two limits, in Fig. 3C–K, we consider three different realizations of  $f_{Na}$  and  $f_K$  (65, 66). For each realization, we show two cross-sections of the phase diagram: one for  $L/\sqrt{D} \rightarrow 0$  and one for  $L/\sqrt{D} \rightarrow \infty$ . Fig. 3D–F shows an example of ion channels for which the effective single cell ( $L/\sqrt{D} \rightarrow 0$ ) exhibits spikes but the weakly coupled interface ( $L/\sqrt{D} \rightarrow \infty$ ) does not. Moreover, Fig. 3G–I

shows an example in which the interface exhibits spikes for all values of  $r$ , yet no ratio of the amplifier and suppressor gives rise to spiking in a single cell.

**Global Bistabilities Underlie Edge Spiking.** In both the interfacial and boundary systems, the presence of spikes is associated with topologically robust features of the underlying dynamical system governed by their respective reaction–diffusion equations. Both Eqs. 3 and 4 and Eqs. 5 and 6 take the form:

$$\dot{A} = D\nabla^2 A + f(A, B, x), \quad [7]$$

$$\dot{B} = \frac{1}{\tau}g(A, B), \quad [8]$$

where  $A(x, t)$  is a fast field and  $B(x, t)$  is a slow field. We will call  $[A_0(x), B_0(x)]$  a stationary solution of Eqs. 7 and 8 if they satisfy  $\dot{A} = \dot{B} = 0$ . Each stationary solution comes paired with a functional  $\Phi$ :

$$\Phi[A] = \int D(\partial_x A)^2 - U(A, x) dx, \quad [9]$$

where  $U(A, x) = \int_0^A f(A', B_0(x), x) dA'$ . The meaning of  $\Phi$  is as follows. If the system is prepared at the stationary solution and the variable  $A$  is perturbed, then on short time scales,  $\dot{A} \approx -\delta\Phi/\delta A$ .

The number of stationary solutions and the critical points of their associated functionals encode the ability of a system to spike. For instance, suppose Eqs. 7 and 8 permit only one stationary solution,  $[A_0(x), B_0(x)]$ , and the associated functional  $\Phi$  only has one minimum [namely  $A_0(x)$ ]. Then, the system will not exhibit spikes because any perturbation to  $A(x)$  quickly relaxes to  $A_0(x)$ . However, if  $\Phi$  permits a second minimum  $A_1(x)$  in addition to  $A_0(x)$ , then the system is excitable: Suitable perturbations to  $A$  will push the system into the basin of attraction of  $A_1(x)$  and, only on longer times ( $t \propto \tau$ ), will the system return to  $A_0(x)$ . Oscillations (i.e., repeated spikes) occur when  $A_0(x)$  itself is a saddle, rather than a minimum, of  $\Phi$ . The number of critical points and their unstable dimensions are topologically robust quantities: These integers are unchanged under sufficiently small, generic perturbations to Eqs. 7 and 8.

For certain models, such as the electrophysiology equations [Eqs. 5 and 6] in the experimentally relevant limit of  $h_\infty(V) = r\Theta(V_* - V)$ , the stationary solutions and associated critical points are captured by a relatively simple geometric construction. The stationary solution for the membrane potential  $V_0(x)$  is constructed as follows: First draw potentials for  $f_K(V)$  (red) and  $h_\infty(V)f_{Na}(V)$  (blue) and align their maxima as shown in Fig. 4A. Treating these as hills, let a ball roll from the top of one hill to the other. The trajectory of the ball in time corresponds to the voltage profile  $V_0(x)$  in space (Fig. 4B). As we show in SI Appendix section 2, the existence of spiking at the interface is determined by an auxiliary function  $X(V)$  defined in Fig. 4C: Place the ball at an arbitrary voltage  $V_R$  and let it roll down the blue hill. The function  $X(V_R)$  is the amount of time it takes for the ball to reach the intersection. Each solution to the equation  $X(V_*) = X(V)$  constitutes a critical point of  $\Phi(V)$ . Whenever  $X(V_*) = X(V)$  has multiple solutions, the system exhibits spikes. As shown in Fig. 4D–F, the precise form of the spikes (excitable vs oscillatory) depends on whether the solution  $V_0(x)$  is stable (excitable) or unstable (oscillatory). Using homological techniques from Conley index theory (67, 68), we show in SI Appendix that the decreasing branch of  $X(V)$  must always be unstable, while the increasing

<sup>†</sup>For simplicity, in this example, we are using the same hopping rate  $\epsilon$  within the forest as between the forest and desert. This distinction becomes irrelevant in the continuum limit (large  $\epsilon$  and large  $N$ ) because this subextensive heterogeneity is absorbed into the Dirichlet boundary condition at an edge or into the continuity requirements across an interface.



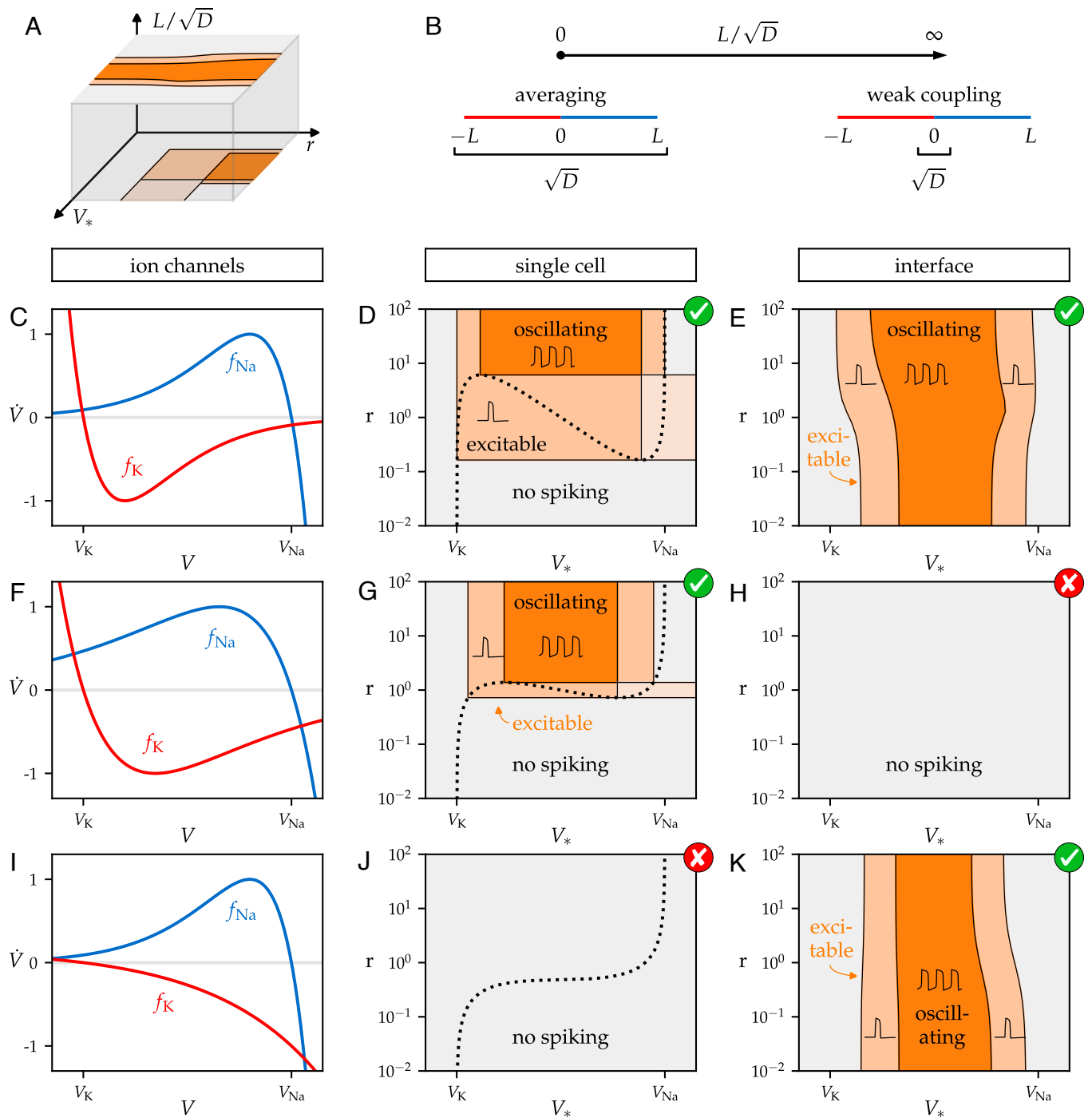


**Fig. 3.** A spiking interface is more than the sum of its parts. (A) A spiking phase diagram is shown for the bioelectric interface in Eqs. 5 and 6. Here,  $L/\sqrt{D}$  is the ratio of the system size to the diffusion length and  $r$  and  $V_*$  appear in  $h_\infty(V) = r\Theta(V_* - V)$ . The parameter  $r$  is the ratio of the amplifier (sodium channel) strength to the suppressor (potassium channel) strength. (B) At small  $L/\sqrt{D}$ , diffusion forces the membrane potential to be approximately constant across the entire tissue, creating an effective single cell with both ion channels. For large  $L/\sqrt{D}$ , the coupling is weak, so the dynamics are spatially heterogeneous. (C–K) A table comparing the  $L/\sqrt{D} \rightarrow 0$  (single cell) and the  $L/\sqrt{D} \rightarrow \infty$  (interfacial) limits. The *Left* column (C, F, and I) shows three examples of voltage-current curves for potassium (red) and sodium (blue) ion channels. Their reversal potentials are denoted  $V_K$  and  $V_{Na}$ , respectively. The *Center* column (D, G and J) contains phase diagrams for  $L/\sqrt{D} \rightarrow 0$ , corresponding to a single cell with both ion channels. The phase boundaries are determined by the dashed line  $h_{eq} = -f_K/f_{Na}$ . In order of brightness, the regions are oscillating, excitable, bistable, and no spiking. If  $h_{eq}$  is monotonic, then the single cell does not exhibit spikes. The *Rightmost* column (E, H and K) contains phase diagrams in the limit  $L/\sqrt{D} \rightarrow \infty$ , describing interfacial dynamics. Row 1 (C–E) shows an example of ion channels in which both the single cell and the interfacial phase diagrams exhibit spiking, but boundaries differ. Row 2 (F–H) shows an example of ion channels for which the single-cell phase diagram contains spiking, while the interfacial phase diagram does not. Row 3 (I–K) shows an example of ion channels for which the interface exhibits spiking, but no ratio  $r$  of the amplifier and suppressor gives rise to spiking in a single cell. The green checks and red crosses indicate phase diagrams that do or do not contain spiking, respectively.

branches are stable. The function  $X(V)$  can be thought of as the high dimensional counterpart of the dashed lines,  $h_{eq}$ , in Fig. 3 D, G and J that determine the phase diagrams for a single cell.

An analogous function  $X(q)$  demarcates the phase boundaries for the predator–prey diagram shown in Fig. 2H; see *Materials and Methods*, section B.

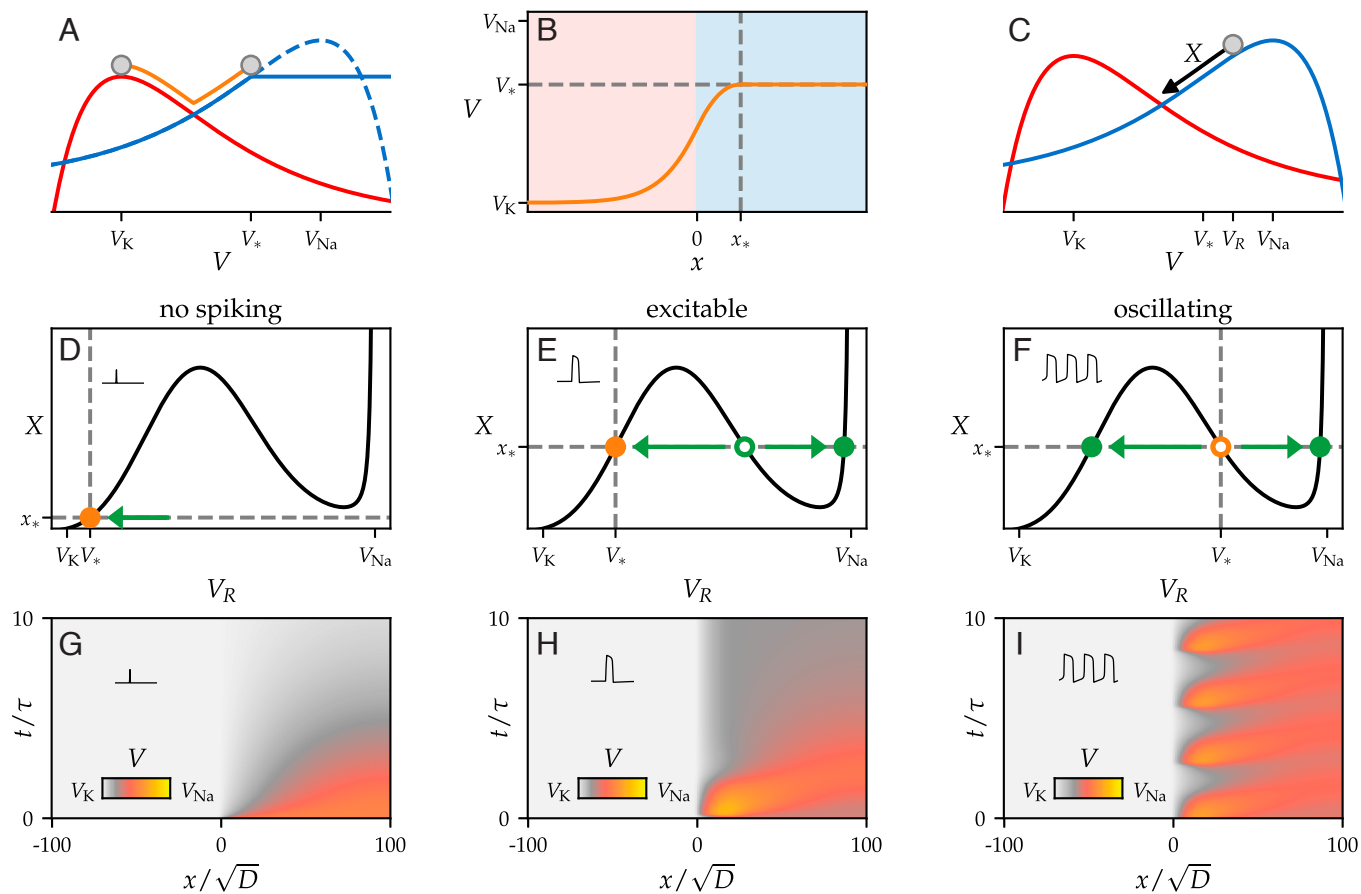


**Fig. 4.** A geometric construction for interfacial spiking. (A) Starting from Eqs. 5 and 6, the antiderivatives of  $f_K(V)$  (solid red line) and  $h_\infty(V)f_{Na}(V)$  (solid blue line) are visualized as hills. The dashed blue line is the antiderivative of  $rf_{Na}(V)$ . To construct the stationary solution with no-flux boundary conditions, consider letting a ball roll from the top of one hill to the other (orange curve). (B) The stationary voltage solution  $V_0(x)$  in space corresponds to the trajectory of a ball (in time) rolling across the potentials in (A). (C) The ability to spike is determined by the number and stability of critical points of  $\Phi$  in Eq. 9. To determine the critical points, we release a ball from a voltage  $V_R$  and measure the “time”  $X$  it takes to reach the intersection. (D) We plot  $X$  as a function of  $V_R$ , and three cases emerge. When  $x_*$  intersects  $X$  once, the interface is unable to spike. (E) When  $x_*$  intersects  $X$  three times and  $V_*$  corresponds to an increasing branch of  $X$ , the interface is excitable. (F) When  $x_*$  intersects 3 times and  $V_*$  corresponds to the decreasing branch, the voltage at the interface oscillates. (G–I) Kymographs illustrating no spiking, excitability, and oscillating at the interface. See *SI Appendix section 5* for simulation details.

**Spiking Mode Transitions and Wave Delocalization.** So far, we have considered bulk media that alone cannot spike but exhibit excitability or oscillations when a boundary or interface is introduced. Now we show that boundaries or interfaces can cause conversions between different modes of spiking. As illustrated in Fig. 1C, we consider two chemical reservoirs separated by a semi-permeable membrane. The reaction in the right chamber ( $x > 0$ ) contains two catalysts with concentrations  $a(x, t)$  and  $b(x, t)$  that evolve according to the Oregonator model of the celebrated Belousov–Zhabotinsky reaction (69). We assume that the catalyst  $a$  is free to diffuse across the interface, while the catalyst  $b$  is relatively immobile. In the left reservoir, the catalyst  $a$  is rapidly converted into a product that exits the reaction. Starting from a minimal chemical reaction network and applying the law of mass action (*SI Appendix section 3*), we derive the following dynamical equations:

$$\dot{a} = D\nabla^2 a + \begin{cases} -a & x < 0 \\ 2m_1 b - a[b_\infty(a) + m_2] & x > 0, \end{cases} \quad [10]$$

$$\dot{b} = \frac{b_\infty(a) - b}{\tau}, \quad [11]$$

where  $m_1$  and  $m_2$  are parameters set by internal rate constants, and  $b_\infty(a)$  is a monotonically decaying function given in

*SI Appendix, Eq. S69*. For sufficiently large  $m_1$  and small  $m_2$ , neither of the reservoirs alone can oscillate. The kymograph in Fig. 1C shows that allowing catalyst  $a$  to diffuse between the two reservoirs creates spontaneous oscillations at the interface. However, unlike the previous examples (predator–prey and electrophysiology), the chamber on the right alone is excitable (though not oscillatory) even without the interface (*SI Appendix, Fig. S4*). The presence of excitability for  $x > 0$  changes a qualitative feature of the oscillations: The interfacial spikes are no longer spatially localized. Instead of dying off at large  $x$  (as in Fig. 1B), the spikes generated at the interface propagate at constant amplitude to the far away boundary (Fig. 1C). Oscillations at chemical interfaces have been reported previously, but they often rely on a distinct mechanism in which chemicals mix at the interface to reach locally suitable conditions for oscillations (70, 71). Interfacial spiking, for example, using gels or other tailored chemistry (72–75), may serve as a promising alternative technique for spatial control of chemical reactions because the two reservoirs can remain distinct indefinitely.

**2D Systems and Nonlinear Waveguides.** In two dimensions, an interface is a 1D line. If the interface is excitable, then the 1D line can host nonlinear waves called trigger waves, as illustrated by the bioelectric experiments in Fig. 1A. In the notation of

Eqs. 7 and 8, an interfacial trigger wave is described by a profile  $A(x, y, t) = A(x, y - ct)$  where  $x$  runs transverse to the interface,  $y$  runs parallel to the interface, and  $c$  is the wave speed. In a  $\tau \rightarrow \infty$  approximation, the sharp front along the interface is described by:

$$D\partial_y^2 A = -c\partial_y A + \frac{\delta\Phi}{\delta A}, \quad [12]$$

which is a higher dimensional version of the profile equation for standard trigger waves (30). When the interface is excitable,  $\Phi$  has two minima, the stationary solution  $A_0(x)$ , and an additional minimum  $A_1(x)$ . In the simplest approximation,  $A_0(x)$  and  $A_1(x)$  are the boundary conditions of Eq. 12 as  $y \rightarrow +\infty$  and  $-\infty$ , respectively. Trigger-wave propagation can then be understood by a classic rolling ball analogy (31): Eq. 12 describes a ball of mass  $D$  moving with damping  $c$  between two maxima [ $A_0(x)$  and  $A_1(x)$ ] of a potential  $-\Phi$ . The front moves in the direction that expands the low potential (larger  $\Phi$ ) region, and the wave speed  $c$  corresponds to the (unique) value of dissipation that allows the ball to arrive at rest on top of the lower peak of  $-\Phi$ . Notably, a sufficiently strong perturbation can create a small region with  $A(x, y) = A_1(x)$  in an otherwise undisturbed undisturbed profile [ $A(x, y) = A_0(x)$ ]. If  $\Phi[A_1] > \Phi[A_0]$ , then the  $A_1$  will expand with trigger waves propagating outward in both directions. If  $\Phi[A_1] < \Phi[A_0]$ , then the initial perturbation will close, and the trigger waves will not propagate.

Geometric primitives, such as curves, corners, and junctions, can then be used to control the propagation of these nonlinear waves. For instance, Fig. 5 *A* and *B* shows a four-way junction formed by patterning two different materials (light and dark gray). In panel (*A*), two trigger waves approach the junction from below. Since the trigger waves are in phase, they interfere constructively and pass through the junction. However, when the pulses are sent periodically with a phase lag (*B*), no pulse passes through due to overlap in their refractory periods. Since the trigger waves are nonlinear, constructive interference results in outgoing waves that have the same amplitude as the incoming waves (rather than twice the amplitude). This modification to the superposition principle can form the basis of more complex devices, such as those capable of computation (76–79). As an illustration, Fig. 5 *C* and *D* and [Movie S2](#) show a two-dimensional (2D) surface patterned by two materials obeying equations of the form of Eqs. 5 and 6. The network of excitable interfaces forms an effective circuit that computes the sum of two binary numbers (see [SI Appendix section 4](#) for additional minimal logic gates, such as AND, OR, and NOT gates). Since only diffusion is required at the boundary, interfacial excitability is potentially useful as a form of wave control that does not require electronics, additional materials, or the fabrication precision necessary to explicitly construct a narrow channel or wire.

## Discussion

Exciting possibilities await in systems with multiple fast degrees of freedom. In this case, the fast dynamics need not be gradient-like and therefore may give rise to more complex interfacial effects like bursting, in which oscillations transiently turn on and off. Likewise, we envision extensions to three-dimensional systems in which the interface is a 2D surface. In addition to engineered waveguides, interfacial spikes may mediate biological functions, such as intracellular chemical signaling (29, 30, 33, 34), as well as pathologies such as atrial fibrillation (80, 81), in which erroneous pacemaking emerges, for example, at the boundary of the aortal and pulmonary heart tissues.

## Materials and Methods

**A. Spike Generation in Fast-Slow Systems without Spatial Extent.** Here, we review examples of spike generation in fast-slow systems without spatial extent. We consider equations of the form:

$$\dot{A} = f(A, B), \quad [13]$$

$$\dot{B} = \frac{1}{\tau}g(A, B), \quad [14]$$

and we assume that  $\tau \gg 1$ , which implies that  $A$  is a fast variable and  $B$  is a slow variable. Fig. 6 *A, Top* shows two curves known as nullclines, which are defined by  $\dot{A} = 0$  (black) and  $\dot{B} = 0$  (gray). The intersection of the nullclines (solid orange circle), denoted  $(A_0, B_0)$ , is a fixed point of Eqs. 13 and 14. If an external stimulus (light blue arrow) pushes  $A$  across a threshold value (open green circle),  $A$  will evolve along the solid green line toward a high value (solid green circle), while  $B$  remains approximately constant. Over a longer period of time, known as the refractory period,  $A$  and  $B$  will move along the dashed orange line back toward their rest position (solid orange circle). This is an example of an excitable system, in which the fast variable  $A$  needs to be stimulated above a critical threshold in order to undergo a spike. Fig. 6 *A, Bottom* shows an equivalent description of the spike: When initially perturbed,  $A$  will evolve according to  $\dot{A} = -\partial_A U$ , where  $\partial_A U(A) = -f(A, B_0)$ . From this perspective, the system is excitable because  $U$  has a minimum (solid green circle) other than the one at  $A_0$  (solid orange circle).

Fig. 6*B* shows a similar example where the fixed point  $(A_0, B_0)$  is unstable. Since the global fixed point is unstable, this system contains a limit cycle denoted by the dashed orange line. Such a system exhibits repeated spikes even in the absence of external stimulation, which we refer to as oscillation or pacemaking. In the following sections, we use an analogous fast-slow decomposition in a high-dimensional setting to identify spiking in reaction-diffusion equations, where the potential  $U$  is replaced by a functional  $\Phi$  of the spatially extended fields.

**B. Phase Diagram for Spiking at a Dirichlet Boundary.** In this section, we provide the mathematical derivations underlying the spiking phase diagram for systems with a Dirichlet boundary, e.g., Fig. 2*H*. In [SI Appendix](#), we generalize the argument to interfaces and apply it to specific systems (i.e., population dynamics, bioelectric tissues, and chemical oscillators).

**B.1. General setting.** Here, we derive the phase diagram featured in Fig. 2*H*. The equations we consider take the form:

$$\dot{A} = \nabla^2 A + B\tilde{f}(A), \quad [15]$$

$$\dot{B} = \frac{1}{\tau}g(A, B). \quad [16]$$

Notice that Eqs. 15 and 16 are a specialization of Eqs. 7 and 8 with  $f(A, B, x) = B\tilde{f}(A)$ . We will assume that  $\tilde{f}(A) > 0$  for  $A \in [0, 1)$  and that  $\tilde{f}$  crosses zero at  $A = 1$ . Moreover, we will assume that there is a function  $0 \leq B_\infty(A) \leq 1$  such that  $g(A, B) < 0$  whenever  $B_\infty(A) < B < 1$  and  $g(A, B) > 0$  whenever  $0 < B < B_\infty(A)$ . We note that  $B_\infty(A)$  is the unique solution to  $g(A, B) = 0$  with  $0 < B < 1$ , and  $B_\infty$  is a zero crossing rather than a local minimum of  $g$ . We will require the boundary conditions  $A(0) = 0$  and  $\partial_x A|_\ell = 0$ . Here,  $\ell = L/\sqrt{D}$  is the nondimensionalized system size. We will assume that the maximum value of  $\tilde{f}$  and  $g$  are of order 1 and that  $\tau \gg 1$ , implying that  $B$  is a slow variable. As we will illustrate with examples in subsequent sections, this form is general enough to capture a wide range of dynamical systems through suitable variable changes.

The calculations below comprise the following steps: We first find the fixed points of Eqs. 15 and 16, which we refer to as stationary solutions. Setting  $\dot{B} = 0$  in Eq. 16 yields  $B = B_\infty(A)$ , and then setting  $\dot{A} = 0$  in Eq. 15 yields the following ordinary differential equation for  $A$ :

$$\nabla^2 A = -B_\infty(A) \frac{dU}{dA}, \quad [17]$$

where  $U$  is an antiderivative of  $\tilde{f}$ . Suppose the system is initialized to a stationary solution, given by  $A_0(x)$  and  $B_0(x) = B_\infty(A_0(x))$ , and suppose the fast field

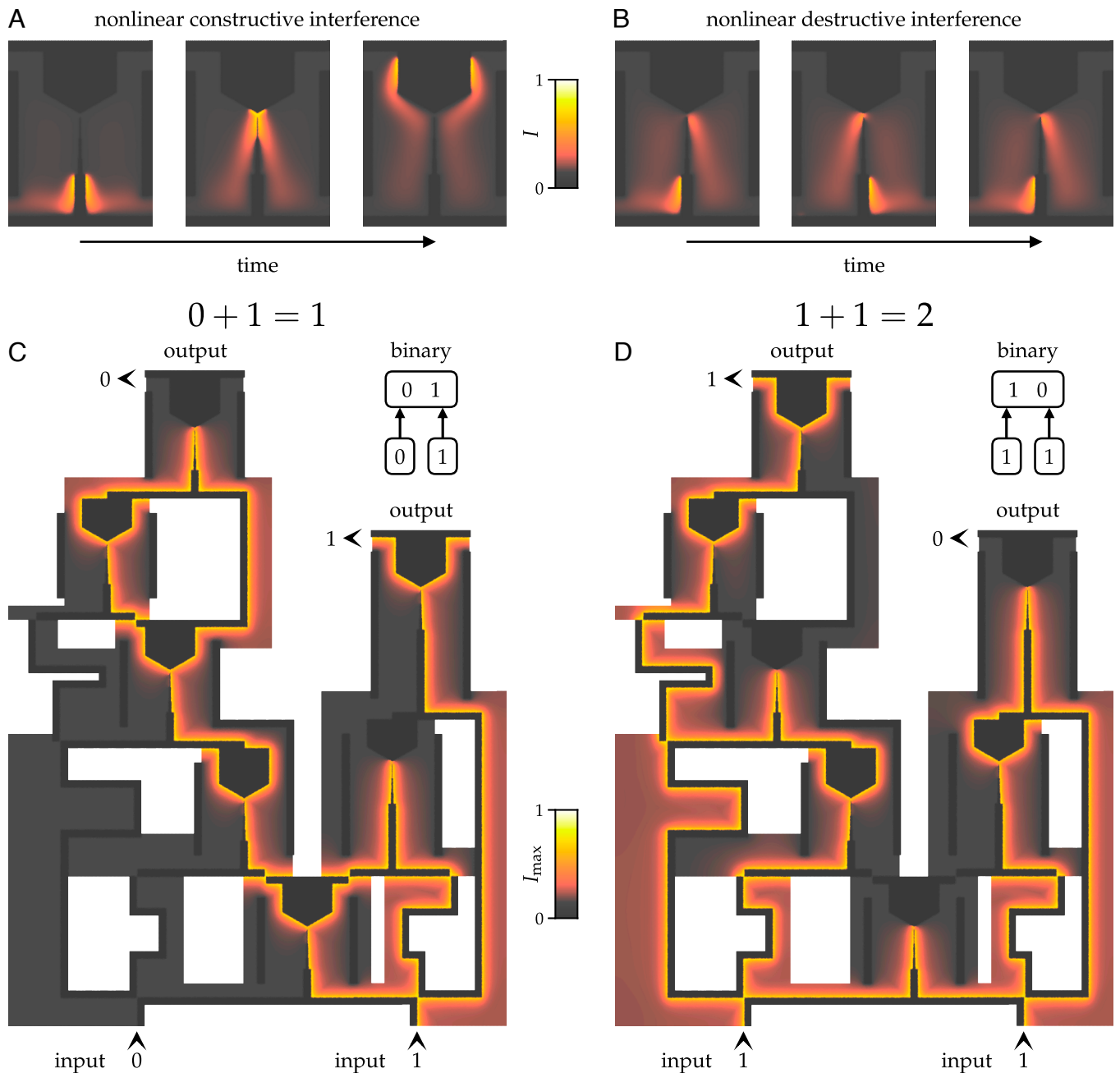


**Fig. 5.** Nonlinear waveguides from interfacial spiking. (A and B) Two distinct non-spiking materials (light and dark gray) are patterned to form a four-way junction of excitable interfaces. When two nonlinear wave trains arrive at a junction in-phase (A), they propagate through uninterrupted. When the two wave trains arrive out-of-phase, they annihilate at the junction. The color corresponds to the intensity  $I$  of the fast, diffusively coupled variable. (C and D) A network of excitable interfaces acts as a binary half adder, which takes the sum of two 0 or 1 inputs. Here, the presence of a wave indicates the value 1, while the absence of a wave indicates the value 0. The color  $I_{\max}$  is the maximum value of  $I$  over time when the network has reached steady state. See [SI Appendix section 4](#) and [Movie S2](#) for more information, and [SI Appendix section 5](#) for simulation details.

$A$  is subject to a perturbation  $A(x, t = 0) = A_0(x) + \delta A(x)$ , where  $\delta A$  is not necessarily small. On short time scales,  $B(x, t)$  will be frozen to  $B_0(x)$  and  $A$  will evolve according to:

$$\dot{A} = \nabla^2 A + B_0(x)\tilde{f}(A) = -\frac{\delta\Phi}{\delta A}, \quad [18]$$

where

$$\Phi = \int_0^\ell [(\nabla A)^2 - B_0(x)U(A)]dA. \quad [19]$$

Solutions to Eq. 18 with  $\dot{A} = 0$  are critical points of  $\Phi$ . Notice that  $A_0(x)$  is always one of the critical points. We will make inferences about the qualitative

behavior of Eqs. 15 and 16 using the structure of the stationary solutions, critical points, and orbits connecting them. Examples of such inferences are as follows:

- Suppose that Eqs. 15 and 16 only permit one stationary solution, and this stationary solution is linearly stable. If the associated  $\Phi$  has no additional critical points beyond  $A_0(x)$ , then the system cannot exhibit spikes because  $A(x, t)$  will quickly return to  $A_0(x)$  after any perturbation.
- Suppose that Eqs. 15 and 16 only permit one stationary solution, and this stationary solution is linearly stable. If  $\Phi$  has stable critical points other than  $A_0(x)$ , then the system is excitable. Namely, if the initial trigger  $\delta A(x)$  pushes the system into the basin of attraction of a second stable critical point, then  $A(x, t)$  will be attracted to the second critical point on a fast time scale ( $t \ll \tau$ )



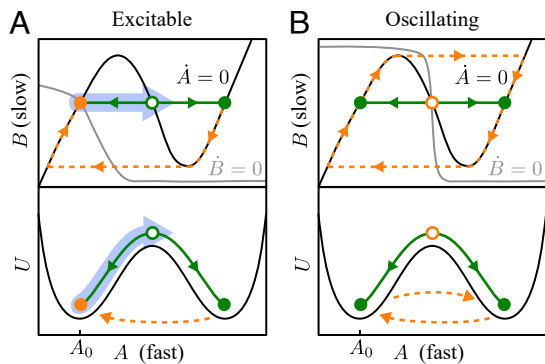


**Fig. 6.** Spike generation in fast-slow systems without spatial extent. (A, Top) A phase portrait of an excitable fast-slow system. The black curve corresponds to  $\dot{A} = 0$ , and the gray curve corresponds to  $\dot{B} = 0$ . The light blue arrow represents an external perturbation. The solid green curves are the fast trajectory, and the dashed orange curve is the refractory period. The solid orange circle denotes the global fixed point. The open (closed) green circle represents an unstable (stable) fixed point of the fast dynamics. (Bottom) On short time scales, the potential  $U(A)$  governs the dynamics. The system is excitable since  $U(A)$  has multiple minima. (B, Top) A phase portrait of a fast-slow system exhibiting oscillations. The dashed orange curve is a limit cycle. The open orange circle denotes an unstable global fixed point. The closed green circles are stable fixed points of the fast dynamics if initialized at the open orange circle. (Bottom) On short time scales, the potential  $U(A)$  governs the dynamics. The system exhibits oscillations since  $U(A)$  has multiple minima, and the orange circle (global fixed point) is not one of them.

and remain there for a long time ( $t \propto \tau$ ) until the slow variable  $B(x, t)$  begins to evolve. This constitutes a spike.

- Suppose that Eqs. 15 and 16 only permit one stationary solution, and this stationary solution is linearly unstable. Assuming chaotic behavior does not occur, the system will (generally) contain a limit cycle. The presence of this limit cycle corresponds to oscillatory activity.
- Eqs. 15 and 16 may have multiple stable stationary solutions. In this case, we refer to the dynamics as multistable.

In the next section, we specialize the form of  $B_\infty(A)$  to allow for an analytical calculation of the stationary solutions and critical points and thereby an analytical construction of a spiking phase diagram.

**B.2. Construction of the phase diagram.** In this section, we specialize the form of  $B_\infty(A)$  to  $B_\infty(A) = \Theta(A_* - A)$ , where  $\Theta$  is the Heaviside step function. Then, Eq. 17 becomes:

$$\nabla^2 A = -\Theta(A_* - A) \frac{dU}{dA} = \frac{dU_{\text{clip}}}{dA}, \quad [20]$$

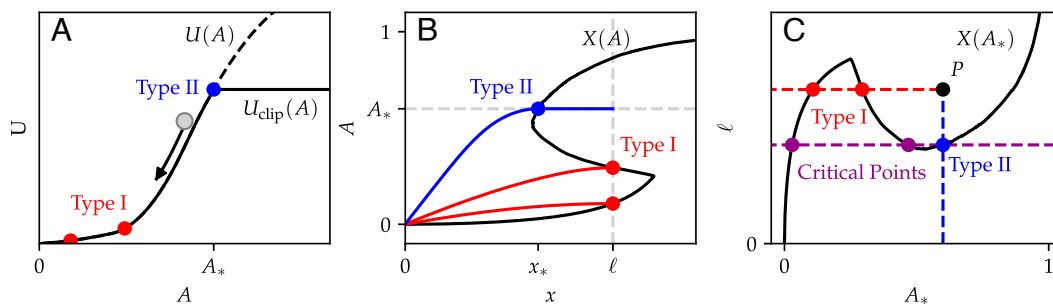


**Fig. 7.** Stationary solutions and critical points. (A) The potentials  $U(A)$  and  $U_{\text{clip}}(A)$  are depicted by dashed and solid lines, respectively. The red points correspond to type I stationary solutions that lie along the non-clipped part of the potential. The blue point corresponds to a type II stationary solution, which lies at the point  $A_*$ . The gray circle symbolizes a ball moving this 1D potential. If released from rest at either of the red points, the ball will take a “time”  $\ell$  to reach  $A = 0$ . If the ball is released from the blue point, it will take a “time”  $X(A_*)$  to reach the origin. (B) The stationary solutions are plotted in real space. Type I solutions intersect the curve  $X(A)$  along the  $x = \ell$  boundary and type II solutions intersect the curve  $X(A)$  along the  $A = A_*$  boundary. (C) The  $(A_*, \ell)$  parameter space is shown, with  $X(A_*)$  plotted. A specific choice of parameters corresponds to a point  $P$ . Type I stationary solutions lie along the dashed red line, while type II lie along the dashed blue line. The critical points associated with the blue stationary solution are indicated with purple circles.

where  $\frac{dU_{\text{clip}}}{dA} = \Theta(A_* - A)\tilde{f}(A)$  defines a potential that has been clipped by the step function; see the solid black line in Fig. 7A. To construct solutions, notice that Eq. 20 is equivalent to the equation of motion for a ball moving in a 1D potential, where  $x$  corresponds to “time” and  $A$  corresponds to “position.” The boundary condition  $\partial_x A|_\ell = 0$  is the requirement that the ball is at rest at “time”  $\ell$ . Likewise, the boundary condition  $A(0) = 0$  is the requirement that the ball reaches “position” 0 at “time” 0. As shown in Fig. 7A, solutions to Eq. 20 can be constructed as follows: Release the ball from rest at point  $A$ , allow it to move through the potential, and measure the amount of “time” it takes to reach point  $A = 0$ . If that “time” is equal to  $\ell$ , then one will have constructed a valid solution to Eq. 20.

Fig. 7A demonstrates that there are two possible types of solutions. For type I (red), the ball is released along the non-clipped part of the potential ( $A < A_*$ ). For type II, the ball is released at  $A = A_*$ : If the amount of “time”  $T$  it takes the ball to reach  $A = 0$  is less than  $\ell$ , then a valid solution can be constructed by letting the ball sit at rest on the flat part of the potential for a “time”  $\ell - T$  before releasing it. In Fig. 7B, the two types of solutions are shown in real space.

To help count the number of solutions to Eq. 20, we introduce a function  $X(A)$  that corresponds to the amount of “time” the ball takes to reach “position” 0 if released from “position”  $A$ . This is given by:

$$X(A) = \frac{1}{\sqrt{2}} \int_0^A \frac{1}{\sqrt{U(a) - U(a')}} da'. \quad [21]$$

Fig. 7B and C show an example of  $X(A)$  featuring one local maximum and one local minimum. Depending on the choice of  $\tilde{f}(A)$ , the function  $X(A)$  can have many local maxima and minima. Nevertheless, the assumptions that  $\tilde{f}(1) = 0$  and  $\tilde{f}(A) > 0$  for  $A < 1$  imply that  $X(A) > 0$ ,  $X(0) = 0$  and  $X(1) = \infty$ . In terms of  $X(A)$ , type I and type II solutions correspond to the following:

*Type I:* If  $a < A_*$  and  $X(a) = \ell$ , then there is a solution with  $A(\ell) = a$ . In this case, the stationary solution  $A(x)$  is given by the inverse of:

$$x(A) = \frac{1}{\sqrt{2}} \int_0^A \frac{1}{\sqrt{U(a) - U(a')}} da'. \quad [22]$$

*Type II:* Let  $x_* = X(A_*)$ . If  $x_* < \ell$ , then there is a solution with  $A(\ell) = A_*$ . In this case, the stationary solution  $A(x)$  can be defined in a piecewise manner:  $A(x) = A_*$  for  $x \in [x_*, \ell]$ ; For  $x < x_*$ ,  $A(x)$  is the inverse of:

$$x(A) = \frac{1}{\sqrt{2}} \int_0^A \frac{1}{\sqrt{U(A_*) - U(a')}} da'. \quad [23]$$

Now, we can think of  $A_*$  and  $\ell$  as being parameters of our dynamical system defined by Eqs. 15 and 16. Working in the  $A_*$ - $\ell$  plane, all the stationary solutions can be found by the graphical construction illustrated in Fig. 7C:

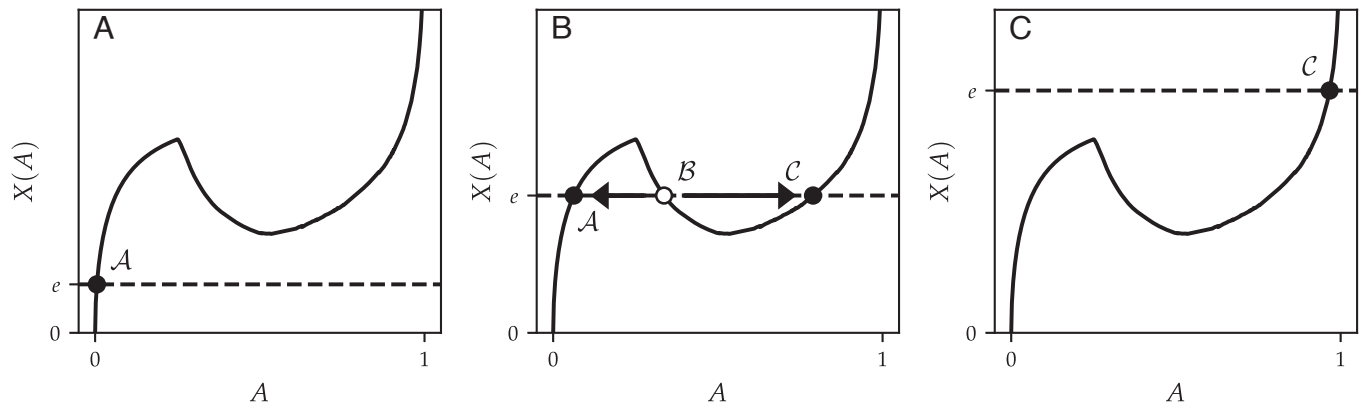


**Fig. 8.** Determining the stability of critical points. The critical points of  $\Phi(A; e)$  are shown for three values of  $e$ . (A) At low  $e$ , there exists only one critical point,  $\mathcal{A}$ . (B) At moderate  $e$ , there exist three critical points  $\mathcal{A}$ ,  $\mathcal{B}$ , and  $\mathcal{C}$ . The solid arrows indicate heteroclinic orbits. (C) At large  $e$ , only one critical point ( $\mathcal{C}$ ) remains. Critical points  $\mathcal{A}$  and  $\mathcal{C}$  must be minima (i.e., unstable dimension of 0), while  $\mathcal{B}$  has an unstable dimension of 1.

1. Represent a choice of parameters  $(A_*, \ell)$  as a point  $P$  in the plane.
2. Draw the curve  $X(A_*)$ .
3. Draw a horizontal line extending to the left from  $P$ . The intersections between the horizontal line and  $X(A_*)$  correspond to stationary solutions of type I.
4. Draw a vertical line extending downward from  $P$ . Intersections between the vertical line and  $X(A_*)$  represent stationary solutions of type II.

This construction yields all the solutions to Eq. 20. Next, we derive the stability of the stationary solutions and their consequences for spiking. To do so, we will specialize to the situation in which  $X(A)$  is "N"-shaped, i.e., it has exactly one local maximum and one local minimum. We will use the following result: Consider the functional:

$$\Phi(A; e) = \int_0^e [(\nabla A)^2 - U(A)] dx, \quad [24]$$

which is minimized with respect to  $A$  subject to the boundary conditions  $A(0) = 0$  and  $\partial_x A|_e = 0$ . Using a similar derivation to that above, one sees that the critical points of  $\Phi$  correspond to the intersections between  $X(a)$  and the horizontal line at  $e$ . As illustrated in Fig. 8A, for sufficiently small  $e$ , there is only one critical point (denoted  $\mathcal{A}$ ) and therefore this critical point must be a minimum of  $\Phi$ . As  $e$  increases (Fig. 8B), a bifurcation produces two new critical points,  $\mathcal{B}$  and  $\mathcal{C}$ . As  $e$  increases further,  $\mathcal{B}$  and  $\mathcal{A}$  annihilate (Fig. 8C). Since  $\mathcal{C}$  is now the lone remaining critical point, it must also be a minimum of  $\Phi$ . Conley

index theory states that two critical points that emerge or annihilate must have unstable dimensions that differ by 1 (67). Since the minima  $\mathcal{A}$  and  $\mathcal{C}$  have an unstable dimension of 0, the unstable dimension of  $\mathcal{B}$  is 1. Moreover, the dynamical system  $\dot{A} = -\frac{\delta\Phi}{\delta A}$  must have heteroclinic orbits from  $\mathcal{B}$  to  $\mathcal{A}$  and  $\mathcal{B}$  to  $\mathcal{C}$ . (See SI Appendix section 7 for a brief introduction to Conley index theory and a derivation of these facts.)

We now apply these facts to deduce the stability of the stationary solutions. For stationary solutions  $A_0(x)$  of type I,  $B_\infty(A_0(x)) = 1$ . Therefore, the fast dynamics for a type I stationary solution are governed by the equation:

$$\dot{A} = \nabla^2 A + \frac{dU}{dA} = -\frac{\delta\Phi_I}{\delta A}. \quad [25]$$

For stationary solutions  $A_0(x)$  of type II,  $B_\infty(A_0(x)) = \Theta(x - x_*)$ , where  $x_* = X(A_*)$ . Hence, the fast dynamics are governed by the equation:

$$\dot{A} = \nabla^2 A + \Theta(x - x_*) \frac{dU}{dA} = -\frac{\delta\Phi_{II}}{\delta A}. \quad [26]$$

Notice that the critical points of  $\Phi_I(A)$  and  $\Phi_{II}(A)$  can be put in correspondence with  $\Phi(A; \ell)$  and  $\Phi(A; x_*)$ , respectively. Therefore, one can use the following graphical construction, illustrated in Fig. 7C, to find the critical points associated with each stationary solution:

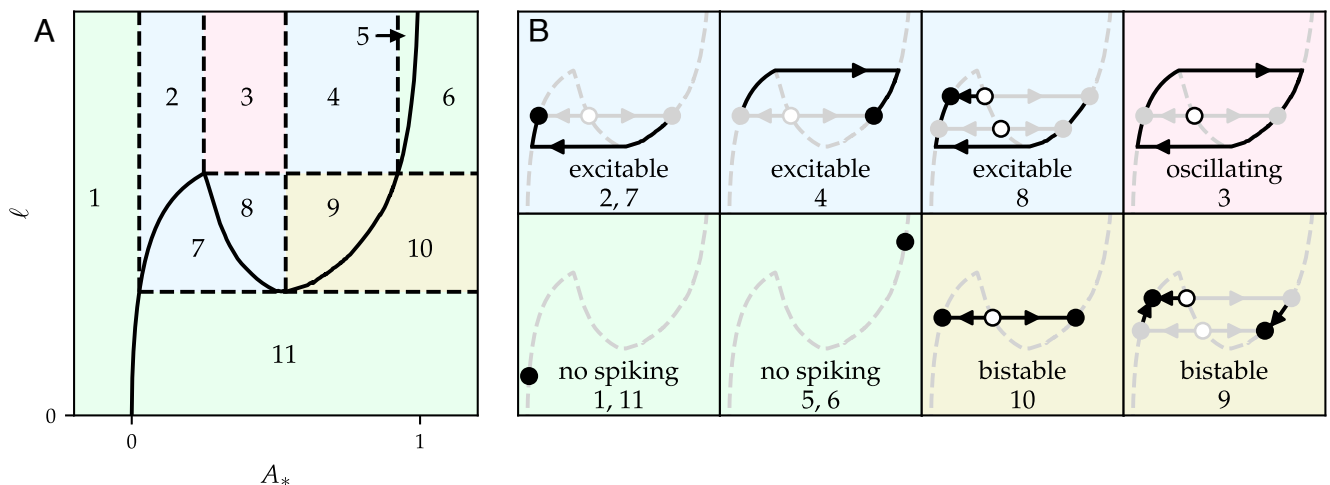


**Fig. 9.** Phase diagram for spiking at a Dirichlet boundary. (A) A phase diagram in the  $A_*$ - $\ell$  plane is divided into 11 distinct regions. The solid black curve is  $X(A_*)$ . The color code indicates the qualitative behavior. Green: no spiking; olive: bistable; blue: excitable; pink: oscillating. (B) The qualitative behavior may be inferred from diagrams that summarize the topological features of the flow. In each diagram, the black circles represent stationary solutions, and the gray circles represent the critical points of the associated potentials. Solid circles are stable, and the open circles are unstable. The light gray lines represent heteroclinic orbits in the fast dynamics, and the black lines convey the evolution of the system on longer time scales.

1. Identify the point corresponding to the stationary solution of interest. (In Fig. 7C, the blue stationary solution is of interest).
2. Draw a horizontal line in both directions out from the point. (Dashed purple line in Fig. 7C).
3. The intersections between the horizontal line and  $X(A_*)$  correspond to critical points. (The blue and purple points in Fig. 7C).
4. The stability of each critical point is determined by which branch of  $X(A_*)$  it lies on: Those on an increasing branch are stable while those on a decreasing branch have an unstable dimension of 1.

Notice that all stationary solutions are also critical points of their associated potential. Occasionally, critical points of one stationary solution are also stationary solutions unto themselves.

These considerations allow us to construct the phase diagram shown in Fig. 9A. The parameter space has been divided into 11 regions based on the number of type I and type II stationary solutions and the nature of their associated critical points. For each region, one can construct a corresponding diagram shown in Fig. 9B. In each diagram, the black circles denote stationary solutions, while gray circles denote critical points that are not stationary solutions. Solid circles indicate stable stationary solutions/critical points, while open circles indicate unstable stationary solutions/critical points. The solid gray lines indicate heteroclinic orbits in the fast dynamics, while the solid black curves depict the evolution of the system over longer time scales.

Using these diagrams, we can then classify distinct qualitative behaviors. Regions 1, 5, 6, and 11 are classified as no-spiking because they feature only one stationary solution, and the functional associated with that stationary solution has only one critical point. Regions 2, 4, 7, and 8 are classified as excitable because they have exactly one stable stationary solution, and the potential associated with this stationary solution has multiple stable critical points. Region 3 is classified as oscillating because it features only one stationary solution, and this stationary solution is unstable, and hence the system exhibits a limit cycle. Regions 9 and 10 are classified as bistable because they feature two stable stationary solutions.

1. A. T. Winfree, Electrical turbulence in three-dimensional heart muscle. *Science* **266**, 1003–1006 (1994).
2. D. M. Bers, Cardiac excitation-contraction coupling. *Nature* **415**, 198–205 (2002).
3. K. H. W. J. ten Tusscher, D. Noble, P. J. Noble, A. V. Panfilov, A model for human ventricular tissue. *Am. J. Physiol.-Heart Circul. Physiol.* **286**, H1573–H1589 (2004).
4. H. Cheng, W. J. Lederer, M. B. Cannell, Calcium sparks: Elementary events underlying excitation-contraction coupling in heart muscle. *Science* **262**, 740–744 (1993).
5. M. Stern, Theory of excitation-contraction coupling in cardiac muscle. *Biophys. J.* **63**, 497–517 (1992).
6. F. X. Witkowski *et al.*, Spatiotemporal evolution of ventricular fibrillation. *Nature* **392**, 78–82 (1998).
7. F. Rieke, D. Warland, R. De Ruyter van Steveninck, W. Bialek, *Spikes: Exploring the Neural Code* (Bradford Book/MIT Press, 1997).
8. B. Drossel, F. Schwabl, Self-organized critical forest-fire model. *Phys. Rev. Lett.* **69**, 1629–1632 (1992).
9. R. M. Anderson, R. M. May, Population biology of infectious diseases: Part I. *Nature* **280**, 361–367 (1979).
10. J. D. Murray, E. A. Stanley, D. L. Brown, On the spatial spread of rabies among foxes. *Proc. R. Soc. London. Ser. B. Biol. Sci.* **229**, 111–150 (1986).
11. R. M. Anderson, H. C. Jackson, R. M. May, A. M. Smith, Population dynamics of fox rabies in Europe. *Nature* **289**, 765–771 (1981).
12. P. Rohani, D. J. D. Earn, B. T. Grenfell, Opposite patterns of synchrony in sympatric disease metapopulations. *Science* **286**, 968–971 (1999).
13. S. Kondo, T. Miura, Reaction-diffusion model as a framework for understanding biological pattern formation. *Science* **329**, 1616–1620 (2010).
14. J. A. Bourret, R. G. Lincoln, B. H. Carpenter, Fungal endogenous rhythms expressed by spiral figures. *Science* **166**, 763–764 (1969).
15. M. Loose, E. Fischer-Friedrich, J. Ries, K. Kruse, P. Schwillke, Spatial regulators for bacterial cell division self-organize into surface waves in vitro. *Science* **320**, 789–792 (2008).
16. N. Tompkins *et al.*, Testing Turing's theory of morphogenesis in chemical cells. *Proc. Natl. Acad. Sci. U.S.A.* **111**, 4397–4402 (2014).
17. H. H. Rotermund, W. Engel, M. Kordesch, G. Ertl, Imaging of spatio-temporal pattern evolution during carbon monoxide oxidation on platinum. *Nature* **343**, 355–357 (1990).
18. O. Steinbock, P. Kettunen, K. Showalter, Anisotropy and spiral organizing centers in patterned excitable media. *Science* **269**, 1857–1860 (1995).
19. M. Vinson, S. Mironov, S. Mulvey, A. Pertsov, Control of spatial orientation and lifetime of scroll rings in excitable media. *Nature* **386**, 477–480 (1997).
20. Y. Fuseya, H. Katsuno, K. Behnia, A. Kapitulnik, Nanoscale Turing patterns in a bismuth monolayer. *Nat. Phys.* **17**, 1031–1036 (2021).
21. T. H. Tan *et al.*, Topological turbulence in the membrane of a living cell. *Nat. Phys.* **16**, 657–662 (2020).
22. A. T. Winfree, Persistent tangled vortex rings in generic excitable media. *Nature* **371**, 233–236 (1994).
23. W. Van Saarloos, V. Vitelli, Z. Zeravcic, *Soft Matter: Concepts, Phenomena and Applications* (Princeton University Press, 2023).
24. A. M. Turing, The chemical basis of morphogenesis. *Philos. Trans. R. Soc. London. Ser. B, Biol. Sci.* **237**, 37–72 (1952).
25. A. Nakamasu, G. Takahashi, A. Kanbe, S. Kondo, Interactions between zebrafish pigment cells responsible for the generation of Turing patterns. *Proc. Natl. Acad. Sci. U.S.A.* **106**, 8429–8434 (2009).
26. S. Kondo, R. Asai, A reaction-diffusion wave on the skin of the marine angelfish *Pomacanthus*. *Nature* **376**, 765–768 (1995).
27. S. A. Newman, H. L. Frisch, Dynamics of skeletal pattern formation in developing chick limb. *Science* **205**, 662–668 (1979).
28. N. P. Mitchell *et al.*, Visceral organ morphogenesis via calcium-patterned muscle constrictions. *eLife* **11**, e77355 (2022).
29. M. C. Wiggers *et al.*, A hierarchy of protein patterns robustly decodes cell shape information. *Nat. Phys.* **17**, 578–584 (2021).
30. S. Di Talia, M. Vergassola, Waves in embryonic development. *Annu. Rev. Biophys.* **51**, 327–353, PMID: 35119944 (2022).
31. M. Vergassola, V. E. Deneke, S. D. Talia, Mitotic waves in the early embryogenesis of *Drosophila*: Bistability traded for speed. *Proc. Natl. Acad. Sci. U.S.A.* **115**, E2165–E2174 (2018).
32. J. Lechleiter, S. Girard, E. Peralta, D. Clapham, Spiral calcium wave propagation and annihilation in *Xenopus laevis* oocytes. *Science* **252**, 123–126 (1991).
33. J. B. Michaux, F. B. Robin, W. M. McFadden, E. M. Munro, Excitable RhoA dynamics drive pulsed contractions in the early *C. elegans* embryo. *J. Cell Biol.* **217**, 4230–4252 (2018).
34. J. B. Chang, J. E. Ferrell Jr., Mitotic trigger waves and the spatial coordination of the *Xenopus* cell cycle. *Nature* **500**, 603–607 (2013).
35. J. M. Davidenko, A. V. Pertsov, R. Salomonsz, W. Baxter, J. Jalife, Stationary and drifting spiral waves of excitation in isolated cardiac muscle. *Nature* **355**, 349–351 (1992).
36. R. A. Gray, A. M. Pertsov, J. Jalife, Spatial and temporal organization during cardiac fibrillation. *Nature* **392**, 75–78 (1998).
37. F. H. Fenton, E. M. Cherry, H. M. Hastings, S. J. Evans, Multiple mechanisms of spiral wave breakup in a model of cardiac electrical activity. *Chaos: Interdiscip. J. Nonlinear Sci.* **12**, 852–892 (2002).
38. J. Halatek, E. Frey, Rethinking pattern formation in reaction-diffusion systems. *Nat. Phys.* **14**, 507–514 (2018).
39. M. C. Cross, P. C. Hohenberg, Pattern formation outside of equilibrium. *Rev. Mod. Phys.* **65**, 851–1112 (1993).
40. M. Kim *et al.*, Controlling chemical turbulence by global delayed feedback: Pattern formation in catalytic CO oxidation on Pt(110). *Science* **292**, 1357–1360 (2001).

Notice that this phase diagram differs at small  $A_*$  from the one shown in Fig. 2H, because  $\tilde{f}$  in the lumberjack-tree setting has an additional zero at  $A = 0$ . In *SI Appendix section 1*, it is explained how the phase diagram in Fig. 9A is mapped onto the one for population dynamics in Fig. 2H.

**Data, Materials, and Software Availability.** All data and code supporting this article are available in Zenodo (DOI: [10.5281/zenodo.10426295](https://doi.org/10.5281/zenodo.10426295)) (62).

**ACKNOWLEDGMENTS.** We would like to thank William Bialek, Ned Wingreen, Joshua W. Shaevitz, David J. Schwab, James P. Sethna, Itai Cohen, Eric R. Dufresne, Erwin Frey, Fridtjof Brauns, Pankaj Mehta, Mary Silber, Brent Dorion, Massimo Vergassola, Suraj Shankar, Noah P. Mitchell, Danny S. Seara, Michel Fruchart, and Tali Khain for useful discussions. C.S. acknowledges support from the Bloomenthal Fellowship and the NSF Graduate Research Fellowship under Grant No. 1746045. V.V. acknowledges support from the Simons Foundation, the Army Research Office under grants W911NF-22-2-0109 and W911NF-23-1-0212, and the University of Chicago Materials Research Science and Engineering Center, which is funded by the NSF under Award No. DMR-2011854. This research was also supported from the National Science Foundation under grant DMR-2118415 and through the Center for Living Systems (grant no. 2317138). A.E.C. acknowledges support from a Vannevar Bush Faculty Fellowship grant N00014-18-1-2859, and NSF Quantum Sensing for Biophysics and Bioengineering (QuBBE) Quantum Leap Challenge Institute (QLCI) grant OMA-2121044. H.O. acknowledges support from an European Molecular Biology Organization (EMBO) Fellowship ALTF 543-2020.

Author affiliations: <sup>a</sup>Department of Physics and The James Franck Institute, The University of Chicago, Chicago, IL 60637; <sup>b</sup>Kadanoff Center for Theoretical Physics, The University of Chicago, Chicago, IL 60637; <sup>c</sup>Department of Chemistry and Chemical Biology, Harvard University, Cambridge, MA 02138; <sup>d</sup>Department of Physics, Harvard University, Cambridge, MA 02138; and <sup>e</sup>Institute for Biophysical Dynamics, The University of Chicago, Chicago, IL 60637

41. F. Brauns, J. Halatek, E. Frey, Phase-space geometry of mass-conserving reaction-diffusion dynamics. *Phys. Rev. X* **10**, 041036 (2020).
42. S. Alonso, F. Sagués, A. S. Mikhailov, Taming Winfree turbulence of scroll waves in excitable media. *Science* **299**, 1722–1725 (2003).
43. H. M. McNamara *et al.*, Bioelectrical domain walls in homogeneous tissues. *Nat. Phys.* **16**, 357–364 (2020).
44. T. Eckstein, E. Vidal-Henriquez, A. Gholami, Experimental observation of boundary-driven oscillations in a reaction-diffusion-advection system. *Soft Matter* **16**, 4243–4255 (2020).
45. E. Vidal-Henriquez, V. Zykov, E. Bodenschatz, A. Gholami, Convective instability and boundary driven oscillations in a reaction-diffusion-advection model. *Chaos: Interdiscip. J. Nonlinear Sci.* **27**, 103110 (2017).
46. W. M. Ni, J. Wei, On the location and profile of spike-layer solutions to singularly perturbed semilinear Dirichlet problems. *Commun. Pure Appl. Math.* **48**, 731–768 (1995).
47. G. Bub, A. Shrier, L. Glass, Spiral wave generation in heterogeneous excitable media. *Phys. Rev. Lett.* **88**, 058101 (2002).
48. Z. F. Mainen, T. J. Sejnowski, Influence of dendritic structure on firing pattern in model neocortical neurons. *Nature* **382**, 363–366 (1996).
49. M. C. Wigbers, F. Brauns, T. Hermann, E. Frey, Pattern localization to a domain edge. *Phys. Rev. E* **101**, 022414 (2020).
50. F. Brauns, J. Halatek, E. Frey, Diffusive coupling of two well-mixed compartments elucidates elementary principles of protein-based pattern formation. *Phys. Rev. Res.* **3**, 013258 (2021).
51. G. Bub, A. Shrier, L. Glass, Spiral wave generation in heterogeneous excitable media. *Phys. Rev. Lett.* **88**, 058101 (2002).
52. K. Agladze, J. P. Keener, S. C. Müller, A. Panfilov, Rotating spiral waves created by geometry. *Science* **264**, 1746–1748 (1994).
53. M. F. Staddon, E. M. Munro, S. Banerjee, Pulsatile contractions and pattern formation in excitable actomyosin cortex. *PLoS Comput. Biol.* **18**, 1–21 (2022).
54. S. Luther *et al.*, Low-energy control of electrical turbulence in the heart. *Nature* **475**, 235–239 (2011).
55. A. Murugan, S. Vaikuntanathan, Topologically protected modes in non-equilibrium stochastic systems. *Nat. Commun.* **8**, 13881 (2017).
56. C. L. Kane, T. C. Lubensky, Topological boundary modes in isostatic lattices. *Nat. Phys.* **10**, 39–45 (2014).
57. M. Z. Hasan, C. L. Kane, Colloquium: Topological insulators. *Rev. Mod. Phys.* **82**, 3045–3067 (2010).
58. S. Shankar, A. Souslov, M. J. Bowick, M. C. Marchetti, V. Vitelli, Topological active matter. *Nat. Rev. Phys.* **4**, 380–398 (2022).
59. B. G. ge Chen, N. Upadhyaya, V. Vitelli, Nonlinear conduction via solitons in a topological mechanical insulator. *Proc. Natl. Acad. Sci. U.S.A.* **111**, 13004–13009 (2014).
60. X. Mao, T. C. Lubensky, Maxwell lattices and topological mechanics. *Ann. Rev. Condens. Matter Phys.* **9**, 413–433 (2018).
61. S. D. Huber, Topological mechanics. *Nat. Phys.* **12**, 621–623 (2016).
62. C. Scheibner, H. Ori, A. E. Cohen, V. Vitelli, Code and data for “Spiking at the edge: Excitability at interfaces in reaction-diffusion systems”. Zenodo. <https://doi.org/10.5281/zenodo.10426295>. Deposited 26 December 2023.
63. H. Ori *et al.*, Observation of topological action potentials in engineered tissues. *Nat. Phys.* **19**, 290–296 (2023).
64. R. FitzHugh, Impulses and physiological states in theoretical models of nerve membrane. *Biophys. J.* **1**, 445–466 (1961).
65. C. Xu *et al.*, Computational design of transmembrane pores. *Nature* **585**, 129–134 (2020).
66. J. Payandeh, T. Scheuer, N. Zheng, W. A. Catterall, The crystal structure of a voltage-gated sodium channel. *Nature* **475**, 353–358 (2011).
67. C. C. Conley, J. A. Smoller, *Algebraic and Topological Invariants for Reaction-Diffusion Equations*, J. M. Ball, Eds. (Springer, Netherlands, Dordrecht, 1983), pp. 3–24.
68. K. Mischaikow, M. Mrozek, “Conley index” in *Handbook of Dynamical Systems*, B. Fiedler, Ed. (Elsevier Science, 2002), vol. 2, pp. 393–460.
69. J. J. Tyson, *The Belousov-Zhabotinskii Reaction* (Springer-Verlag, Berlin, New York, 1976).
70. M. A. Budroni, L. Lemaigre, D. M. Escala, A. P. Muñozuri, A. De Wit, Spatially localized chemical patterns around an  $a + b \rightarrow$  oscillator front. *J. Phys. Chem. A* **120**, 851–860 (2016).
71. B. Dúzs, P. De Kepper, I. Szalai, Turing patterns and waves in closed two-layer gel reactors. *ACS Omega* **4**, 3213–3219 (2019).
72. S. N. Semenov *et al.*, Autocatalytic, bistable, oscillatory networks of biologically relevant organic reactions. *Nature* **537**, 656–660 (2016).
73. R. Yoshida, Self-oscillating gels driven by the Belousov-Zhabotinsky reaction as novel smart materials. *Adv. Mater.* **22**, 3463–3483 (2010).
74. G. Rabai, K. Kustin, I. R. Epstein, A systematically designed pH oscillator: The hydrogen peroxide-sulfite-ferrocyanide reaction in a continuous-flow stirred tank reactor. *J. Am. Chem. Soc.* **111**, 3870–3874 (1989).
75. A. Testa *et al.*, Sustained enzymatic activity and flow in crowded protein droplets. *Nat. Commun.* **12**, 6293 (2021).
76. A. Adamatzky, B. De Lacy Costello, T. Asai, *Reaction-Diffusion Computers* (Elsevier Science, 2005).
77. J. Holley, I. Jahan, B. De Lacy Costello, L. Bull, A. Adamatzky, Logical and arithmetic circuits in Belousov-Zhabotinsky encapsulated disks. *Phys. Rev. E* **84**, 056110 (2011).
78. Á. Tóth, K. Showalter, Logic gates in excitable media. *J. Chem. Phys.* **103**, 2058–2066 (1995).
79. O. Steinbock, Á. Tóth, K. Showalter, Navigating complex labyrinths: Optimal paths from chemical waves. *Science* **267**, 868–871 (1995).
80. H. M. McNamara *et al.*, Geometry-dependent arrhythmias in electrically excitable tissues. *Cell Syst.* **7**, 359–370.e6 (2018).
81. E. M. Cherry, J. R. Ehrlich, S. Nattel, F. H. Fenton, Pulmonary vein reentry-properties and size matter: Insights from a computational analysis. *HeartRhythm* **4**, 1553–1562 (2007).